Hydrogen as a fuel additive in laminar premixed methane flames: Impact on the nucleation and growth of soot particles

Hong-Quan Do, Alessandro Faccinetto, Luc-Sy Tran, Pascale Desgroux, Laurent Gasnot, Abderrahman El Bakali, Xavier Mercier

Hydrogen as a fuel additive in laminar premixed methane flames: Impact on the nucleation and growth of soot particles

Hong-Quan Do, Alessandro Faccinetto, Luc-Sy Tran, Pascale Desgroux, Laurent Gasnot, Abderrahman El Bakali*, Xavier Mercier*

Univ. Lille, CNRS, UMR 8522 - PC2A - Physicochimie des Processus de Combustion et de l'Atmosphère, F-59000 Lille, France

Full-Length Article

Supplemental Material (SM) is available:

SM1: Additional information (PDF file)

SM2: Experimental data (Excel file)

* Corresponding authors:

Prof. Dr. Abderrahman El Bakali

Email: abderrahman.el-bakali@univ-lille.fr

Dr. Xavier Mercier

Email: xavier.mercier@univ-lille.fr

Abstract:

This work reports new experimental data regarding the impact of H_2 on slightly sooting methane flames (Φ–1.91) characterized by the formation of soot particles undergoing growth processes. This study has been carried out in three atmospheric sooting premixed methane flames with added H_2 (2% of the total flowrate) or substituted (10% molar comparing to CH_4 fuel).

The mole fraction profiles of selected aliphatic and aromatic compounds (C_1-C_{16}) have been measured by Gas Chromatography and Jet-Cooled Laser-Induced Fluorescence. Concerning the soot particles, we have implemented for the first time an analytical methodology based on in-situ measurements by Laser-induced Incandescence and Cavity Ring-Down Spectroscopy coupled with ex-situ measurements by Scanning Mobility Particle Sizing (SMPS). This original approach allows to determine the soot volume fraction profiles and corresponding evolution of the particle number densities and particles size density function without requiring accurate knowledge of the dilution ratio during SMSP measurements.

The reported data highlight that the introduction of H_2 strongly influences the formation of aromatic species and soot depending on the operating conditions (H_2 addition or substitution). The impact of H_2 was evaluated on the nucleation step and the soot growth processes. In that context, we notably show that the H_2 substitution inhibits while the H_2 addition favors the formation of nascent soot particles, and furthermore the H_2 addition generates substantial modifications in the dynamic of the soot growth processes. This work also supports the idea that the onset of the particle nucleation might be controlled by specific concentration thresholds of aromatic precursors.

Keywords: soot, hydrogen, polycyclic aromatic hydrocarbons (PAHs), soot growth, premixed flame

1. Introduction

Reducing the emissions of soot and gaseous pollutants from the combustion of conventional hydrocarbon fuels is an ongoing challenge. Hydrogen (H_2) is well-known as a zero-carbon energy carrier with low ignition energy and high burning velocity [1–3]. However, the use of H_2 alone in real industrial systems is not yet optimal due to certain inherent handling difficulties and the necessary adaptations of industrial processes. Major safety issues arise from the wide flammability range and low ignition energy of H_2 [4–6]. In this context, H_2-hydrocarbon blends, which are easier to implement in real combustion systems, have received increased attention due to different positive aspects notably related to their increased combustion efficiency and propensity to reduce soot and gaseous pollutant emissions. The local flame extinction, combustion stability and power output of CH_4 combustion have all been shown to be improved by H_2 enrichment [7,8], and the addition of small amounts of H_2 to methane has been demonstrated to increase the performances of gas powered spark-ignited engines [9]. Moreover, the presence of H_2 in synthetic natural gas flame has been shown to inhibit the formation of CO and CO_2 [10].

The impact of H_2 on the formation of soot precursors and soot particles has also been the subject of numerous experimental and modeling studies [11–35]. Regarding soot precursors, the impact of added H_2 (40% in CH_4) in a methane laminar premixed sooting flame (equivalence ratio relative to CH_4 Φ_C=2.2) has notably been shown to enhance the formation of aliphatic C_1-C_4 species as well as benzene and toluene [29]. Ezenwajiaku et *al.* [28] experimentally studied the impact of H_2 (20% in CH_4) on the formation of polycyclic aromatic hydrocarbons (PAHs) in a diffusion flame and concluded that H_2 addition to fuel decreased their concentration.

Haynes et *al.* [25] found that H_2 addition (3% of total flame flowrate) to an ethylene flame operating at the soot inception C/O ratio promoted the formation of nascent soot. By

contrast, Liu et *al*. [30] and Xu et *al*. [31] investigated the effect of H_2 addition (up to 40% comparing to the base fuel) on soot formation in methane diffusion flames and found that the addition of H_2 in these cases strongly decreased the soot volume fraction. This tendency to decreasing the soot volume fraction in flames when adding amounts of H_2 (from 10 up to 50% H_2/fuel) has been observed in numerous works investigating flames stabilized with various fuels as ethane, ethylene, propane, butane [15,17,21,22,24,36,37].

Besides, De Iuliis et *al.* showed that the introduction of H_2 in an ethylene/air premixed flame [24] by a substitution procedure slowed down the soot growth process due to the decrease of the H/H_2 ratio. Choi et *al.* [16] investigated the effect of H_2 addition on the micro- and nano-structure of soot particles in an ethylene/air counter-diffusion flame. They highlighted that H_2 addition decreased the size of the soot microstructures and enhanced the formation of PAHs containing 5 carbon atom rings that induce the curvatures into the carbon lamella.

The effect of H_2 on the number density of soot particles has also been investigated in literature. Tesner et *al.* [14] found that H_2 addition (30% comparing to fuel) to a methane diffusion flame increased the number density of soot particles. Zhao et *al.* [22] mentioned that H_2 addition (20% comparing to fuel) and H_2 substitution (25% of ethylene by H_2) to an ethylene laminar diffusion flame decreased the number density of soot particles by 23% and 66% respectively, comparing to the reference flame. However, the H_2 effect was not only due to the dilution and chemical inhibition but also to the reduced number of carbon atoms in the initial mixture.

Hence, at the state of the art, the literature shows that the introduction of H_2 into sooting flames enhances or inhibits the formation of soot particles and their precursors depending on the operating conditions. We recently also showed that the introduction of H_2 in a nucleation methane flame (Φ_C=1.82), i.e. a flame generating only nascent soot particles [32], drastically reduced or enhanced the formation of aromatic species and the soot volume fraction, depending

on the way of introducing H_2 (either by addition or substitution to the diluent). However, these flames did not allow studying the soot growth process and the impact of H_2 on the soot particles distribution and soot number density.

In the present work, as part of a continuing effort to improve the understanding of the impact of H_2 on soot formation, we investigated the impact of H_2 on a slightly richer methane flame (Φ_C=1.91) characterized by the formation of soot particles undergoing growth processes. As demonstrated by [38], both nucleation and growth process happen simultaneously under fuel-rich flame conditions. These richer operating conditions allowed us to examine the effect of H_2 on both the nucleation and growth processes.

Similarly to our previous work [32], we employed two different approaches to introduce H_2 to the reference methane flame, consisting either in keeping constant (H_2 substitution) or slightly increasing (H_2 addition) the total gas flow rate. We implemented a large panel of experimental methods to record the most complete set of experimental data to gather information on the role of H_2 on these two specific soot formation steps. Hence, we measured the mole fraction profiles of gaseous species including selected aliphatic and aromatic compounds (C_1-C_{16}) in the different flames. Moreover, we determined the soot volume fraction profiles as well as the corresponding evolution of the soot particle size distribution and number density using a combination of complementary highly sensitive analytical tools. To this aim, we developed a new analytical method based on the coupling of laser induced incandescence (LII), cavity ring-down spectroscopy (CRDS) and scanning mobility particle sizing (SMPS) to determine the soot number density from the soot volume fraction and soot particle size distribution measured in the flame.

2. Experiment methods

2.1. Burner and flame conditions

Three atmospheric methane premixed flames were stabilized on a water-cooled McKenna burner equipped with a bronze porous disk (6 cm diameter). The system was already described previously [32]. In the present study, the water in the cooling circuit was kept at 296 K and a shield nitrogen flow, introduced in the co-annular section of the porous disk, was set to 1440 NLPH (normal liter per hour) to prevent perturbations induced by the surrounding air.

As recently reported for nucleation flames [32], two different approaches have been used to introduce H_2 into the reference methane flame, consisting on either keeping constant or slightly increasing the total gas flow rate. The first method consisted of replacing a small amount of dilution nitrogen, equal to 10% of CH_4 flow rate with H_2, hence preserving a total constant flowrate. The corresponding flame is denoted Φ-1.91_H_2-S. The second method consisted of adding the same amount of H_2 directly to the cold gas supply, therefore leading to a slight increase (around 2%) of the total flowrate compared to the reference flame. The corresponding flame is denoted Φ-1.91_H_2-A. The introduction of such a small quantity of H_2 (< 2%) strongly limits its impact on the flame temperature which is an essential parameter in the soot particle formation processes. The experimental conditions of the flames are reported in Table 1.

	Flame		
	Φ-1.91	Φ-1.91_H_2-S	Φ-1.91_H_2-A
Φ_C	1.91	1.91	1.91
Φ_{C+H}	1.91	1.96	1.96
C/O	0.479	0.479	0.479
Total flow rate (NLPH)	690.6	690.1	704.5
x_{CH4}	0.202	0.202	0.198
x_{O2}	0.211	0.211	0.207
x_{N2}	0.587	0.567	0.575
x_{H2}	0	0.020	0.020
$T_{adiabatic}$ (K)	1806	1806	1787
$T_{uncorrected}$ (K)	1552	1569	1543
Flame velocities at 298 K and 1 atm (cm/s)	9.1	9.9	9.2

Table 1. Experimental conditions. Flame name: Φ-1.91: CH_4 flame; Φ-1.91_H_2-S: CH_4 substituted-H_2 flame; Φ-1.91_H_2-A: CH_4 added-H_2 flame. $T_{adiabatic}$: adiabatic temperature calculated using GASEQ program [39]. $T_{uncorrected}$: measured temperature by using a type B thermocouple without radiative heat loss correction. Flame velocities have been calculated using the GRI mechanism [40]. $\Phi_C = 2\ x_{CH4}/\ x_{O2}$ and $\Phi_{C+H} = 2\ x_{CH4}/x_{O2} + 0.5\ x_{H2}/x_{O2}$

2.2. Experimental setup

In this work, several experiments were implemented to measure the flame temperature, the mole fraction profiles of combustion products (CO, CO_2, H_2, H_2O), aliphatic species (C_1-C_6), benzene, naphthalene, pyrene, soot volume fractions, number density of particles as well as particles size density functions (PSDFs) along the flame height.

2.2.1. Flame temperature measurement

The temperature profiles of the three studied flames were measured with a Pt/Rh(6%)-Pt/Rh(30%) type B thermocouple (diameter 100 µm) along the centerline of the flame as a function of the height above the burner (HAB) from 0 mm to 16 mm. The thermocouple was coated with a ceramic layer of BeO–Y_2O_3 to reduce catalytic effects [41]. As the main objective of this measure was only to check whether the temperature profile was modified by the H_2

addition/substitution, no specific correction has been applied to the reported temperature profiles.

2.2.2. Measurement of gaseous species by GC, JCLIF and FTIR

The gaseous species formed in the sooting flames were extracted by a quartz sampling microprobe (350 µm orifice). As described in our previous work [32], gas chromatography (GC) was used to identify and quantify CO, H_2, aliphatic species and benzene. The uncertainty on the mole fraction of gaseous species measured by GC in this study is estimated to be < 5% for major species and < 10% for minor species. Naphthalene and pyrene concentration profiles were determined by jet cooled laser induced fluorescence (JCLIF) while CO_2 and H_2O were measured by Fourier-transform infrared spectroscopy (FTIR). The measurement uncertainty on all these species was estimated < 13%. The C, O and H atomic balances of the three studied flames were found to be close to 100% as detailed in Table S1 of the Supplemental Material 1 (SM1).

2.2.3. Determination of the soot volume fraction profiles by LII and CRDS

Soot volume fraction profiles were determined by laser induced incandescence (LII) measurements calibrated by cavity ring-down spectroscopy (CRDS) according to a procedure already described in previous papers from our group [32,42]. The same method has been employed and adapted to the present work. Hence, only the main details of the setup will be given here.

CRDS experiments were performed by using a Nd:YAG laser (Quantel) generating a laser pulse at 1064 nm. The cavity we used consisted of two identical 25-mm-diameter plano-concave mirrors (radius of curvature: 25 cm) coated to achieve a high reflectivity of R = 99.96% at 1064nm. The mirrors were separated by distance of 40 cm. The burner was

placed at the central position between these two mirrors. A laser pulse was injected inside the cavity with a specific optical system constituted of two lenses and a pinhole in order to preferentially match the TEM00 modes of the cavity. The ring-down time characterizing the lifetime of the laser pulse inside the cavity was recorded thanks to a photomultiplier Hamamatsu R2257 (PMT). A longpass filter (RG-780) was placed in front of the PMT to limit the parasite light due to the flame emission. The lifetime of the laser pulse was then transformed into an extinction value according to a procedure already described elsewhere [32,42]. The measured extinction coefficient $K_{ext} = K_{abs} + K_{sca}$ (K_{abs} and K_{sca} being respectively the absorption and the scattering coefficients) was assumed to be equal to K_{abs} (K_{sca} being negligible).

LII experiments were also carried out by using 1064 nm laser excitation wavelength generating by the same laser used for CRDS experiments. The laser beam was expanded into a collimated horizontal plane using a specific optical system described in details in [32] to provide a top-hat irradiance profile at the position of the LII collection volume. The LII signal was collected at right angle of the laser axis by a system of lenses and a Hamamatsu R2257 PMT positioned behind an entrance slit (0.6 mm vertical × 6 mm horizontal) and an interference filter centered at 532±10 nm in order to limit parasite emission and scattering light from the flame. The LII signals recorded by the PMT were acquired and digitized by an oscilloscope Lecroy HDO - 4104A.

Basically, LII signals can be defined according to *Eq.1*:

$$S_{LII}(\lambda_{em}, T_p(t)) = E(m)\frac{48\pi^2 hc^2}{\lambda_{em}^6}\left[\exp\left(\frac{hc}{\lambda_{em}.k_b.T_p(t)}\right)-1\right]^{-1} f_v(t) \qquad Eq.1$$

where $E(m)$ is the absorption function of the particles, T_p the temperature of the heated soot by the laser pulse, c the speed of light in vacuum, λ_{em} the emission wavelength, k_b the Boltzmann constant, h the Planck constant and f_v the soot volume fraction.

This equation shows a dependence on $E(m)$ and to T_p. In order to determine the LII profiles representative of the evolution of f_v, it is therefore important to consider the evolution of the value of $E(m)$ as well as the heated temperature T_p along the flame height. To this aim, we first determined the fluence curves characterizing the response of the LII signal to laser energy against the HAB in all studied flames. These fluence curves are reported in Fig.1.

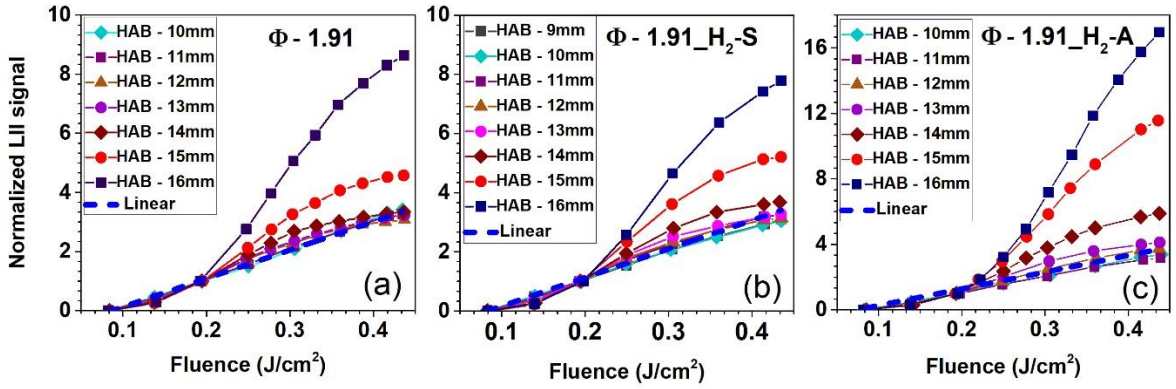

Fig.1: Normalized fluence curves at 0.2 J/cm^2 obtained in three studied flames. Φ-1.91: CH_4 sooting reference flame; Φ-1.91_H_2-S: CH_4 substituted-H_2 flame; Φ-1.91_H_2-A: CH_4 added-H_2 flame.

We arbitrary chose to normalize the LII fluence curves reported in Fig.1 at 0.2 J/cm^2. From this figure, it appears that the evolution of the normalized fluence curves with HAB is relatively similar in the three sooting flames. Hence, we observe that the fluence curves determined at the lowest heights (HAB ≤ 12 mm), show for the three flames a similar quasi-linear evolution over the fluence range accessible with our laser. It has been shown that this behavior is typical of nascent soot particles which are characterized by low $E(m)$ values and require therefore much higher fluence to reach the sublimation threshold [43,44]. Based on

236 recent characterization of optical properties and fluence curves of such particles [42] we used
237 the constant value E(m) = 0.250 ± 0.025 for the soot particles identified as nascent soot particles
238 in our flames, i.e. for HAB up to 12 mm.

239 At higher HAB, the fluence curves are characterized by a more classical S-shape
240 strongly depending on T_p with an inflexion point appearing around 0.4 J cm^{-2} characteristic of
241 the sublimation threshold of more mature soots [45]. This evolution denotes a change of the
242 optical properties of the detected soot particles correlated with an increase of *E(m)*. The value
243 of *E(m)* is indeed well known to vary with the soot maturity in flame [46–50]. Values from 0.2
244 to 0.4 are usually considered in the literature to characterize particles from the nucleation step
245 to the fully mature graphite-like particle [51–53]. The determination of the evolution of the
246 E(m) value with soot maturity along the flame height was beyond the scope of this work and
247 has not been carried out. Based on the literature, we rather chose to consider a constant value
248 *E(m)*=0.300 ± 0.030 as proposed by Yon et *al.* [54] for the more mature soot particles formed
249 from 12.5 mm to 16 mm for all studied flames.

250 All the recorded LII profiles have been measured by using a laser fluence just below the
251 soot sublimation threshold energy determined from these experimental fluence curves to
252 minimize the influence of T_p on the measured LII signal [55]. Based on these considerations,
253 this laser fluence has been defined equal to 0.359 J cm^{-2} for the three flames studied in this
254 work.

255 Finally, LII profiles were calibrated in f_v profiles according to the method already detailed in
256 previous works [32,42] and relying on the measurement of the extinction coefficient K_{ext} carried
257 out by CRDS. This coefficient, defined by the well-known *Eq.2*, has been determined at 16 mm
258 HAB as described in [32,42].

$$K_{ext} = \frac{6\pi E(m)}{\lambda} f_v \qquad \textit{Eq.2}$$

259

Where λ corresponds to the excitation wavelength (1064 nm) used for the extinction measurement.

2.2.4 Characterization of the particles size density functions (PSDFs) by SMPS

To measure the particle size distributions, we used a nano-SMPS system (TSI Inc.) as presented in SM1 (Fig. S1) which is capable of measuring size distributions from 1 to 30 nm, coupled to a sampling system based on dilutive microprobe extraction specifically designed for this SMPS experiments.

Soot particles were extracted from the flames by using a microprobe made of two co-annular quartz tubes, the outer tube ending with a long thin tip with a 250 μm orifice. This probe was positioned vertically and inserted into the flame throughout the burner stabilization plate. The outer tube was used to send a cold nitrogen flow (6 L min^{-1}) enabling a fast dilution of the sampled material from the flame directly at the entrance of the microprobe. The dilution ratio was estimated in the range 500-3000. The inner tube was connected to a pump system allowing the sampling of the diluted flow of particles from the flame. A 2 L buffer volume interposed between the probe and the nano-SMPS was required to stabilize the pressure in the sampling line. This system has been implemented in order to avoid post-sampling chemical reactions as well as coagulation and/or aggregation of the sampled particles.

The polydisperse aerosol was injected in the TSI nano-SMPS consisting, in the order, of: (1) a soft X-ray neutralizer model 3088 to reach a known particle charge distribution function; (2) a differential mobility analyzer (DMA) model 3086 operating over the size range 1-30 nm and controlled by an electrostatic classifier model 3082; (3) a nano-enhancer model 3757 that pre-activates the smallest particles in an environment supersaturated in diethylene glycol, and finally (4) a standard n-butanol condensation particle counter (CPC) model 3570 [56]. To minimize diffusion losses, the highest total flow 2.5 L min^{-1} was used in all experiments and

the sampling line was optimized for minimal distance (<2 m) between the probe and the nano-SMPS [57].

3. Determination of the profiles of the soot particle number densities

To determine the soot particle number density along the flame HAB, we used an original methodology relying on the coupling of the data obtained by SMPS and LII/CRDS measurements. Basically, the SMPS system was used to determine the normalized PSDFs against HAB for the studied flames. The PSDFs were then calibrated into absolute number densities with the soot volume fraction profiles determined by LII and CRDS, according to the analytical procedure explained below. This procedure provides the advantage of not requiring accurate knowledge of the dilution ratio during SMSP measurements, which remains a strong limitation for ex-situ measurements.

It is to be noted that comparisons between f_v deduced from the measurement of the soot PSDFs by SMPS with direct *in situ* extinction measurements have already been reported in the literature and showed very good correlation [58]. The main uncertainty, according to this comparison, has been attributed to the potential variations of the soot refractive index. In our work, the studied flames have been shown to produce soot particles characterized by fluence curves indicating a slight evolution of the optical properties all along the flame height, limiting therefore this issue.

3.1. Theory

The particle size distribution function (PSDF) of soot in the flame sampled volume can be expressed as a function of the particle number density N and the particle diameter D_p as:

$$\frac{dN}{d\log D_\mathrm{p}} = \sum_{\mathrm{i}=1}^{2} N_\mathrm{i}\left(\frac{dN}{d\log D_\mathrm{p}}\right)_\mathrm{i} \qquad \textit{Eq. 3}$$

The sum of functions in *Eq. 3* is necessary to account for the bimodal structure observed at some HAB. N_i is the (partial) particle number density of each mode. The total particle number density is given by:

$$N_\mathrm{tot} = \int_0^\infty \frac{dN}{d\log D_\mathrm{p}} d\log D_\mathrm{p} = N_1 + N_2 \qquad \textit{Eq. 4}$$

$\left(\frac{dN}{d\log D_\mathrm{p}}\right)_\mathrm{i}$ is well represented, as it will become clear in the experimental section, by lognormal distributions having median diameter $\overline{D}_{\mathrm{p,i}}$ and geometric standard deviation $\sigma_{\mathrm{g,i}}$ [59–64]:

$$\left(\frac{dN}{d\log D_\mathrm{p}}\right)_\mathrm{i} = \frac{1}{\sqrt{2\pi}\log\sigma_{\mathrm{g,i}}}\exp\left[-\frac{\left(\log D_\mathrm{p} - \log\overline{D}_{\mathrm{p,i}}\right)^2}{2\left(\log\sigma_{\mathrm{g,i}}\right)^2}\right] \qquad \textit{Eq. 5}$$

It is important to notice that in this work we chose the normalized number density $\frac{dN}{d\log D_\mathrm{p}}$ over $\frac{dN}{dD_\mathrm{p}}$ since the former is independent of the instrument resolution and therefore particularly useful when intercomparing data from different instruments. In the explored D_p range (1.5-15 nm), soot particles are spherical and isolated [55], and the shift between the two representations $\frac{dN}{d\log D_\mathrm{p}}$ and $\frac{dN}{dD_\mathrm{p}}$ is always verified to be < 0.1 nm and thus considered as negligible.

CRDS (in-situ) measures the soot volume fraction f_v without giving access to any information on the PSDF that is hidden in the integral:

$$f_\mathrm{v} = \frac{\pi}{6}\int_0^\infty D_\mathrm{p}^3 \frac{dN}{d\log D_\mathrm{p}} d\log D_\mathrm{p} \qquad \textit{Eq. 6}$$

On the other hand, SMPS (online) accesses the electrical mobility size distribution $\left(\frac{dN}{d\log D_\mathrm{p}}\right)_\mathrm{SMPS}$, but cannot provide a reliable measurement of the in-situ total particle number density that is biased by the sampling:

$$\frac{dN}{d\log D_\mathrm{p}} = K(D_\mathrm{p})\left(\frac{dN}{d\log D_\mathrm{p}}\right)_\mathrm{SMPS} \qquad Eq.\ 7$$

Here, the function $K(D_\mathrm{p})$ folds in all sampling-related effects that include the probe and dilution effects during sampling and the particle losses during transport in the probe, in the sampling line and in the SMPS due to diffusion, and depends on a number of factors including D_p.

In this work, the same probe and dilution flow were used in all experiments. The uncertainty due to the HAB-dependent temperature on the probed flame volume is small and therefore included in the calculation of the total uncertainty of the particle number density. In order to avoid post-sampling coagulation, preliminary SMPS scans were performed at each HAB by decreasing the differential pressure (thus increasing the dilution ratio) until the particle number density was sufficiently low that no shift of the PSDF to higher D_p could be observed in the time required for the data acquisition. All the PSDFs discussed in this work have been acquired with a dilution ratio equal or higher than this limit.

The quantitative estimation of the particle losses due to diffusion during transport is difficult and well beyond the scope of this paper. In this work, a rough estimation was performed by following the theoretical approach proposed by Kulkarni et *al*. [65] to calculate the transport efficiency function $\eta_\mathrm{tube,diff}$ against D_p. The calculated $\eta_\mathrm{tube,diff}$ has the highest slope between 2-3 nm, and is roughly twice as large at 5 nm than 2 nm. While experimental estimations of the particle losses for D_p < 10 nm exist in the literature [66,67], they are typically determined for very specific experimental conditions or subject to large uncertainty, and thus

344 often regarded as tricky to generalize. For this reason, and to avoid introducing further
345 uncertainty in the interpretation of the measurements, we decided to discuss the uncorrected
346 SMPS output, thus de facto neglecting the effect of the particle losses due to diffusion that will
347 be instead the object of a future dedicated investigation.

348 Under these assumptions, $K(D_\mathrm{p}) \approx K$ can effectively be treated as a calibration factor
349 for the given experimental conditions. In conclusion, the relationship between f_v from *in-situ*
350 extinction (CRDS) and $\left(\frac{dN}{d\log D_\mathrm{p}}\right)_\mathrm{SMPS}$ from online electrical mobility (SMPS) can be
351 approximated as:

$$f_\mathrm{v} = \frac{\pi}{6} K \int_0^\infty D_\mathrm{p}^3 \left(\frac{dN}{d\log D_\mathrm{p}}\right)_\mathrm{SMPS} d\log D_\mathrm{p} \qquad \textit{Eq. 8}$$

352

353 **3.2. Application of the method**

354 A practical example of the fitting procedure applied to the PSDF measured in the sooting
355 flame Φ-1.91 at 12 mm HAB is shown in Fig. 2.

356

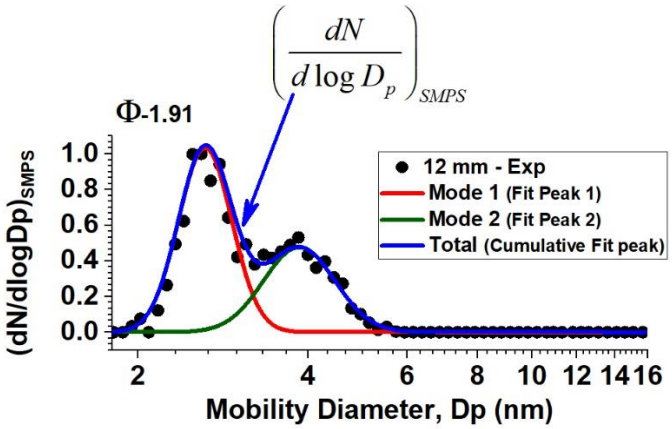

357

358 Fig. 2: Result of the fitting procedure by using two lognormal functions at the onset of the bimodality
359 of size distribution at 12 mm HAB in sooting flame Φ-1.91.

As explained above, the method of determination of the soot number density N_p relies on finding the empirical factor K that enables the calibration of the normalized PSDFs reported in SM1 (Fig. S6) obtained by SMPS into absolute number density, with f_v being known from CRDS experiments. This calibration factor K is defined in *Eq 7* and independently calculated at each sampled HAB. For instance, at 12 mm HAB in the flame Φ-1.91:

$$K_{12\mathrm{mm}} = \frac{f_\mathrm{v}}{\frac{\pi}{6}\int_0^\infty D_\mathrm{p}^3 \left(\frac{dN}{d\log D_\mathrm{p}}\right)_{\mathrm{SMPS}} d\log D_\mathrm{p}} = \frac{1.24\times10^{-10}}{3.74\times10^{-21}} \approx 3.32\times10^{10} \qquad \textit{Eq. 9}$$

The integration of the PSDF allows deducing, according to *Eq. 4*, the total number density of soot particles that in the example at 12 mm HAB: $N_\mathrm{p} = 6.59\times10^9$ cm^{-3}. This protocol can be extended to the determination of the number density of soot particles in the different modes (mode 1 and mode 2) of the PSDF, as graphically shown in Fig. 3 ($N_{\mathrm{p},1} = 4.09\times10^9$ cm^{-3}, in red and $N_{\mathrm{p},2} = 2.50\times10^9$ cm^{-3}, in green).

This procedure has been applied to all the investigated flames to obtain the absolute soot numbers density profiles presented and discussed in the following sections.

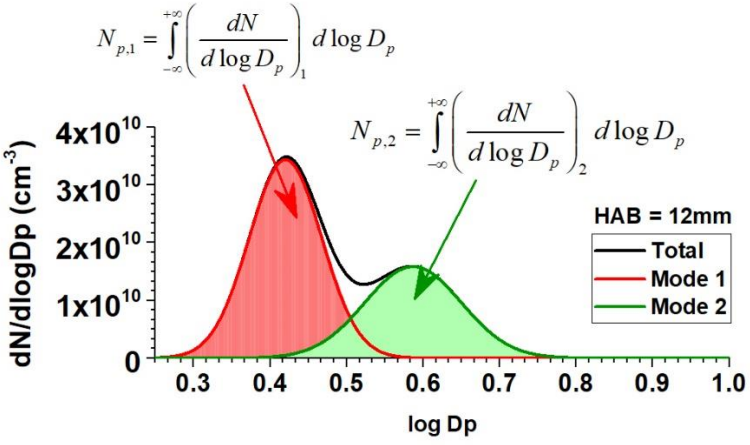

Fig. 3: Determination of number density of mode 1 and 2 of soot particles at 12 mm HAB in the flame Φ-1.91.

4. Results and discussion

4.1. Effect of H_2 on the flame temperature profiles

Fig. 4 displays the experimental temperature profiles obtained with a coated Pt/Rh(6%)-Pt/Rh(30%) thermocouple for the three studied flames (Φ-1.91, Φ-1.91_H_2-S, and Φ-1.91_H_2-A). The reported temperatures were not corrected from the radiative heat loss. As it can be seen, the H_2 substitution (Φ-1.91_H_2-S) shifts the temperature profile toward the burner surface due to the laminar flame velocity increase (see Table 1), while the addition procedure (Φ-1.91_H_2-A) does not cause any shift. Indeed, the laminar flame velocity of flame Φ-1.91_H_2-S has been determined to be around 9.9 m/s which was higher than that calculated in flame Φ-1.91 around 9.2 m/s. By contrast, the laminar flame velocity of flame Φ-1.91_H_2-A around 9.1 m/s is close to that of reference flame Φ-1.91. In both approaches (addition or substitution), as expected by such a small introduction of H_2 (1.8%), all studied flames exhibit similar temperature peak, confirming the negligible influence of the additional H_2. Hence, the temperature measured in the post flame region where soot particles are formed and growing are very close in the three studied flames. The adiabatic temperature calculated using GASEQ [39] confirms the very limited impact of H_2 on the flame temperature profiles as shown in Table 1. The absence of modification in the three measured temperature profiles (except the slight shift towards the burner of the whole profile in the case of H_2 substitution) therefore allows attributing the change of the mole fraction of PAHs and soot volume fraction to the effect of H_2 and not to the temperature.

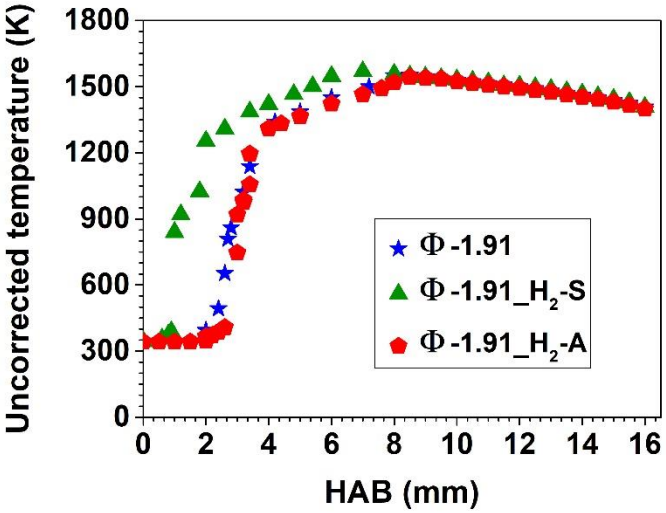

399 Fig. 4: Impact of H_2 on the uncorrected flame temperature profiles. Φ-1.91: CH_4 flame; Φ-1.91_H_2-S:
400 CH_4 substituted-H_2 flame; Φ-1.91_H_2-A: CH_4 added-H_2 flame (see Table 1 for the flame conditions).
401
402 **4.2. Effect of H_2 on major species (reactants and combustion products)**
403 Fig. 5 reports the mole fraction profiles of the main species including reactants (fuel,
404 O_2) and final products (CO, CO_2, H_2, H_2O) for the three studied flames. As observed for the
405 temperature profiles presented above, the H_2 substitution (Φ-1.91_H_2-S) systematically shifts
406 the profiles of the major species around 2 mm closer to the burner surface while the H_2 addition
407 (Φ-1.91_H_2-A) does not significantly modify the flame position. The explanation for this effect
408 is the same as the explanation for the temperature profiles discussed in Section 4.1. Briefly, this
409 shift can be explained by the laminar flame velocity increase in the case of H_2 substitution
410 (Φ-1.91_H_2-S). By contrast, in the case of H_2 addition (Φ-1.91_H_2-A), no significant
411 modification of the flame velocity is calculated and therefore no significant influence on the
412 flame position. It is to be noted that the higher mole fractions of H_2 observed at HABs from
413 0 mm to 11 mm in the latter flame compared to the reference flame are simply due to the added
414 H_2 fraction in the initial gas mixture. The impact of H_2 on the evolution of the mole fraction
415 profiles of the reactants and final products obtained in the three flames is similar as the one
416 observed in the three nucleation flames reported in our recent work [32].

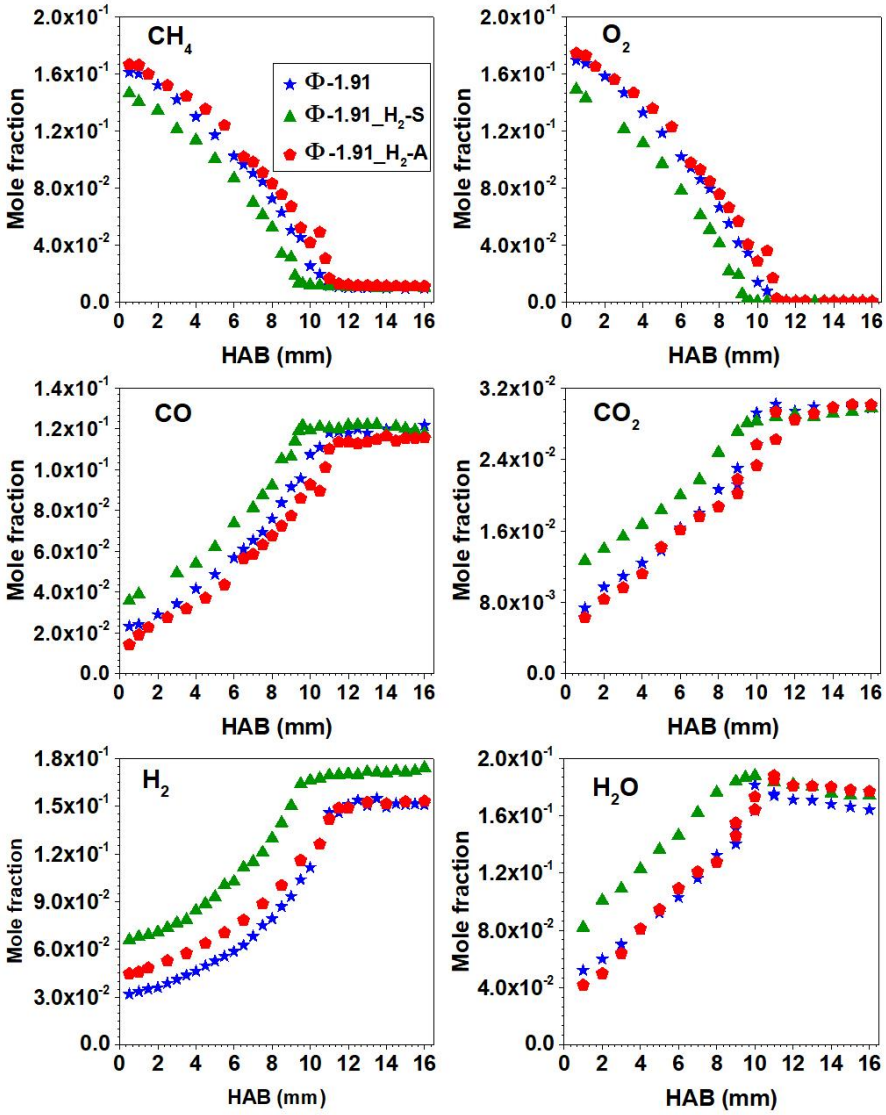

Fig. 5: Mole fraction profiles of reactants (fuel, O_2) and major products (CO, CO_2, H_2, H_2O) obtained in the three studied flames.

4.3. Effect of H_2 on soot precursors

Fig. 6 shows the mole fraction profiles of some aliphatic and aromatic species in the three flames. We present here the mole fraction profiles of acetylene (C_2H_2), allene (AC_3H_4) and propyne (PC_3H_4) which are considered as important precursors of the first aromatic ring, PAHs and soot [68–71]. The mole fraction profiles of other aliphatic species analyzed in this work are available in SM1 (Fig. S2). Fig. 6 also displays the measured mole fraction profiles

of three aromatic compounds (benzene C_6H_6, naphthalene $C_{10}H_8$ and pyrene $C_{16}H_{10}$) which are considered as crucial soot precursors [32,72–74].

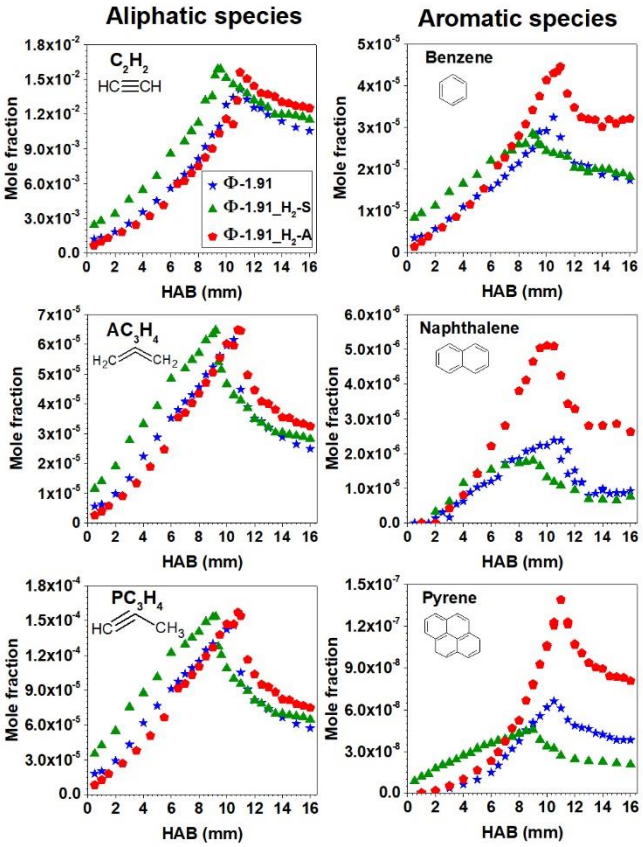

Fig. 6: Mole fraction profiles of aliphatic species (acetylene, allene, propyne) and aromatic species (benzene, naphthalene and pyrene) obtained in the three studied flames.

The H_2 substitution shifts the mole fraction profiles of all gaseous species around 2 mm closer to the burner surface because of the increase of the laminar flame velocity as presented in Table 1, consistently with the consumption behavior, while H_2 addition does not induce any significant effect on the position of the mole fraction profiles of the detected species in the gas phase. Both H_2 substitution and addition show no significant effect on the peak values of the mole fraction of the aliphatic species. However, the presence of H_2 in the sooting flame Φ-1.91 strongly impacts the formation of aromatic species (Fig. 6). The H_2 substitution (Φ-1.91_H_2-S) exhibits an inhibitory effect (12-31%) on benzene, naphthalene, and pyrene formation whereas

the H_2 addition (Φ-1.91_H_2-A) clearly promotes their formation (30-53%). Such antagonistic effect was also observed for the nucleation flames in our recent work [32]. In this work we have also shown that the impact of H_2 can be specifically attributed to a chemical effect rather than dilution. Indeed, substituting the equivalent of 1.8% of N_2 by He did not affect the mole fraction profiles of benzene and aliphatic species in any flames as shown in SM1 (Fig. S3).

A detailed explanation of the chemical effect of H_2 on aromatic species was given in our previous work [32]. The same mechanism could be considered for the present flames, as summarized in Fig. S4. Under flame conditions, H_2 can be converted to H-atoms through several reactions, such as $H_2+OH \rightarrow H+H_2O$, $H_2+O \rightarrow H+OH$, and $H_2+M \rightarrow H+H+M$. The H_2 effect is then the result of different competitive processes that share the resulted H-atoms as a reactant. As showed in Fig. S4 (left panel), the high temperature branching reaction $H + O_2 = O + OH$ (path A) competes with the benzene/PAH accumulation process (path B), the PAH growth processes (path C), and the soot particle growth processes (paths D and E) that are significant in the fuel richer flames. As showed in the right panel of Fig. S4 in the case of substitution, the path A is reinforced by the presence of H_2 which is proved by the observed increase of the laminar flame speed (Table 1). In these conditions, the H-atoms are thus largely converted to OH and O, resulting in the acceleration of the oxidation processes of aromatic species and in the decrease of the H-atoms available for the PAH growth through the HACA mechanism. These points explain the decrease of the mole fractions of the aromatic species under the H_2 substitution conditions.

In the case of H_2 addition, the reaction $H + O_2 = O + OH$ is not favored. This is confirmed by the flame front position and by the calculated laminar flame speed, which highlighted similar values for the flame with added H_2 (Φ-1.91_H_2-A) and the reference flame (Φ-1.91) as reported in Table 1. Thus, H-atoms from H_2 addition would primarily participate to the benzene/PAHs formation by termination reactions, promoting aromatic formation.

4.4. Effect of H_2 on soot formation

The measured soot volume fraction profiles determined for the three studied flames are reported in Fig. 7. The H_2 substitution shifts the soot volume fraction f_v profile around 2 mm closer to the burner surface, while H_2 addition does not induce this effect (Fig. 7a). The effect of H_2 on the position of the f_v profile is consistent with that of the gaseous soot precursors as reported in Fig. 6. The H_2 substitution decreases while H_2 addition increases the maximum f_v. Hence, the impact of H_2 on the soot quantities generated in flame Φ-1.91 may be directly related to the formed PAHs mole fractions as discussed above.

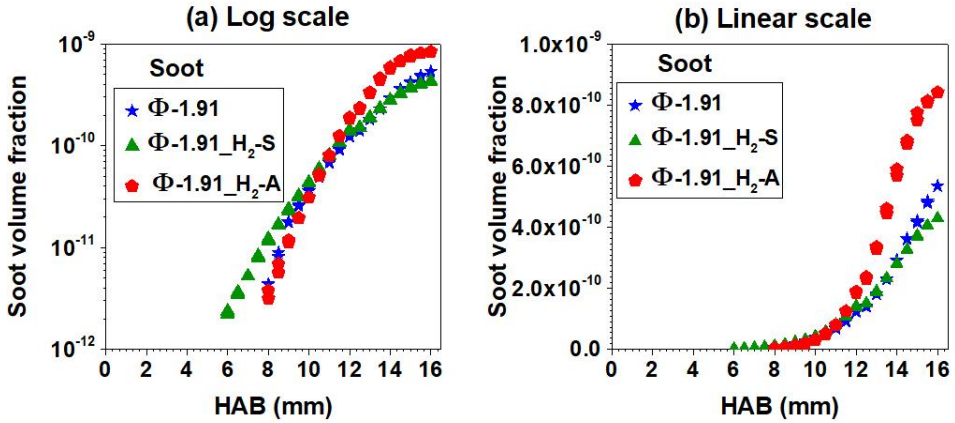

Fig.7: Soot volume fraction profiles measured in the three studied flames by LII /CRDS. (a) log scale and (b) linear scale.

4.4.1. Hypothesis about a PAH concentration threshold for soot nucleation

In flame Φ-1.91_H_2-S, we carefully determined by LII the HAB corresponding to the beginning of the soot formation according to the sensitivity of our optical setup (first measurable LII signals). Hence this point has been established at 6 mm HAB for this flame and the corresponding soot volume fraction at this HAB has been determined to be around 2 ppt, i.e. a value similar to that previously measured at the soot starting point of the nucleation flames

485 [32]. The corresponding mole fractions of benzene, naphthalene and pyrene at this HAB were
486 determined around 22 ppm, 1.5 ppm and 36 ppb, respectively, which are very close to the values
487 measured at the onset of the soot nucleation point of the previously studied nucleation flames
488 [32]. This observation therefore supports the hypothesis already suggested in [32] of a PAH
489 concentration thresholds, potentially independent of the flame operating conditions and nature
490 of the fuel, triggering the soot nucleation process. Unfortunately, the determination of this onset
491 point in the other two flames was affected by higher uncertainty. Regarding our data, and
492 notably the signal-to-noise ratio (SNR) of the LII signal measured at 8 mm, corresponding to
493 the lowest studied HAB by LII in the Φ-1.91 and Φ-1.91_H_2-A flames (Fig S.5b and c), it is
494 clear that the SNR appears much better than that observed at 6 mm in flame Φ-1.91_H_2-S.
495 Hence, it is likely that the onset of the soot nucleation point for these two flames is located a
496 little upstream 8 mm. However, the soot volume fractions determined at 8 mm in the flame
497 Φ-1.91 (f_v=4.4ppt) and flame Φ-1.91_H_2-A (f_v=3.2 ppt) are still very close to that at the onset
498 of the soot nucleation point in flame Φ-1.91_H_2-S (f_v=2 ppt). Moreover, it is noteworthy that
499 the mole fractions reported in Table 2 of benzene, naphthalene and pyrene measured at the onset
500 of the soot nucleation points in the three flames (Φ-1.91 flame, Φ-1.91_H_2-A, Φ-1.91_H_2-A)
501 are similar and also very close those of previously investigated nucleation flames [32] (see also
502 Table 2). These data support therefore the idea of a PAH concentration threshold required to
503 initiate the soot nucleation process. However, it is clear that more experimental work, especially
504 involving other fuels, is required to confirm this hypothesis.
505
506
507
508
509

Flame	Mole fractions (soot starting point)		
	Benzene (ppm)	Naphthalene (ppm)	Pyrene (ppb)
Φ-1.91	21	1.8	38
Φ-1.91_H_2-S	22	1.5	36
Φ-1.91_H_2-A	28	3.8	52
Φ-1.82 / Φ-1.82_H_2-S / Φ-1.82_H_2-A [32]	16	1.3	22

Table 2: Mole fractions of aromatic compounds determined at the onset of the soot nucleation in the three rich flames Φ-1.91 and previously studied nucleation flames Φ-1.82 [32].

4.4.2. Effect of H_2 on the particle size distribution function

In this section, the impact of H_2 on the soot particle diameter and number density and more specifically on its influence on the growth mechanism of soot formation is discussed in detail. Fig. 8 presents the PSDFs measured from SMPS, LII and CRDS experiments against HABs in the three studied flames. As it can be seen in this figure, the first measurable PSDFs by SMPS in these flames appears at slightly higher HABs than the detection of the first LII signals reported in Fig. 7. In the absence of a deepen comparison between the two techniques, it is difficult to conclude about the origin of this small shift, which might be due to several reasons as a lower detection limit of the LII setup or the flame perturbation induced by the probe sampling required for the SMPS measurements. However, this small discrepancy suggests that our microprobe only slightly perturbs the flame front, which validates the complementary use of these techniques implemented here to characterize the soot formation.

Concerning the Φ-1.91 flame, as already observed in the literature [75–77], we notice at the lowest HABs the appearance of a single mode characterized by a fixed diameter all along the flame height, followed by the formation of a second mode higher in the flame, highlighting

the growing particles. The first PSDF measured at 8 mm HAB, that characterizes the nascent soot particles generated in the nucleation process, features a monomodal lognormal distribution centered around 2.5 nm (mode 1). The monomodal distribution exists only up to 10.5 mm HAB. Above 10.5 mm HAB, a bimodal distribution appears. While mode 1 does not shift to higher D_p as the HAB increases, mode 2, newly appeared at 10.5 mm HAB and initially centered at 3.2 nm, shifts to higher D_p as HAB increases. The existence and shift of mode 2 point to the competition between nucleation, coagulation and surface reactions as already well established in the literature [58,77–79]. At 12 mm HAB, mode 2 appears more clearly and mode 1 reaches its maximum intensity. Above 12 mm HAB, mode 1 begins to decrease and disappears completely at 15 mm HAB, suggesting that the nucleation process is no longer active above this HAB probably because of the diminution of the concentration of aromatic soot precursors in the flame. Fig. 9 presents the evolution of the median diameter of mode 1 and 2 against HAB for the three studied flames. We observe that the median diameter of mode 1 is constant against HAB and that the median diameter of mode 2 increases gradually. This dynamic suggests that the soot growth process in flame Φ-1.91 are dominated by the HACA mechanism and by PAHs condensation on the soot surface rather than coagulation/coalescence processes.

Concerning the influence of H_2 (Φ 1.91_H_2-S and Φ 1.91_H_2-A flames), Figs. 8 and 9 show that both H_2 substitution and addition do not influence the PSDF (median diameter and geometric standard deviation) of mode 1. This result indicates that the mechanism of nascent soot formation from gaseous precursors is probably similar in the three studied flames, which will be further discussed in the next section. The end of the nucleation process observed in the Φ-1.91_H_2-S flame at 15 mm HAB is similar to the reference flame Φ-1.91. By contrast, it is noteworthy that the formation of nascent soot particles in flame Φ-1.91_H_2-A is promoted along the whole flame height.

555 Fig. 10 shows the evolution of the soot number density of mode 1, mode 2 and the total
556 soot number density in the three studied flames. H_2 substitution slightly decreases the maximum
557 soot number density of mode 1 while H_2 addition strongly increases this value. This decrease
558 or increase of mode 1 with the H_2 substitution or addition could be a result of a decrease or an
559 increase in the formation of aromatic species, respectively, as shown in Fig. 6. Above 15 mm
560 in the two flames Φ-1.91 and Φ-1.91_H_2-S, the mole fraction of aromatic species is low (Fig.
561 6). Hence, aromatic species can not initiate anymore the soot nucleation process. By contrast,
562 in the Φ-1.91_H_2-A, the H_2 addition strongly increases the formation of aromatic species. In
563 this case, the mole fraction of these species is always above the aromatic concentration
564 threshold associated to the formation of the very first soot particles [32] and this, even for the
565 higher HAB in this flame. In this case, the nucleation process is always active along the flame
566 height in flame Φ-1.91_H_2-A. These data therefore again point out to the need of a minimum
567 concentration of PAHs required for the activation of the soot nucleation process

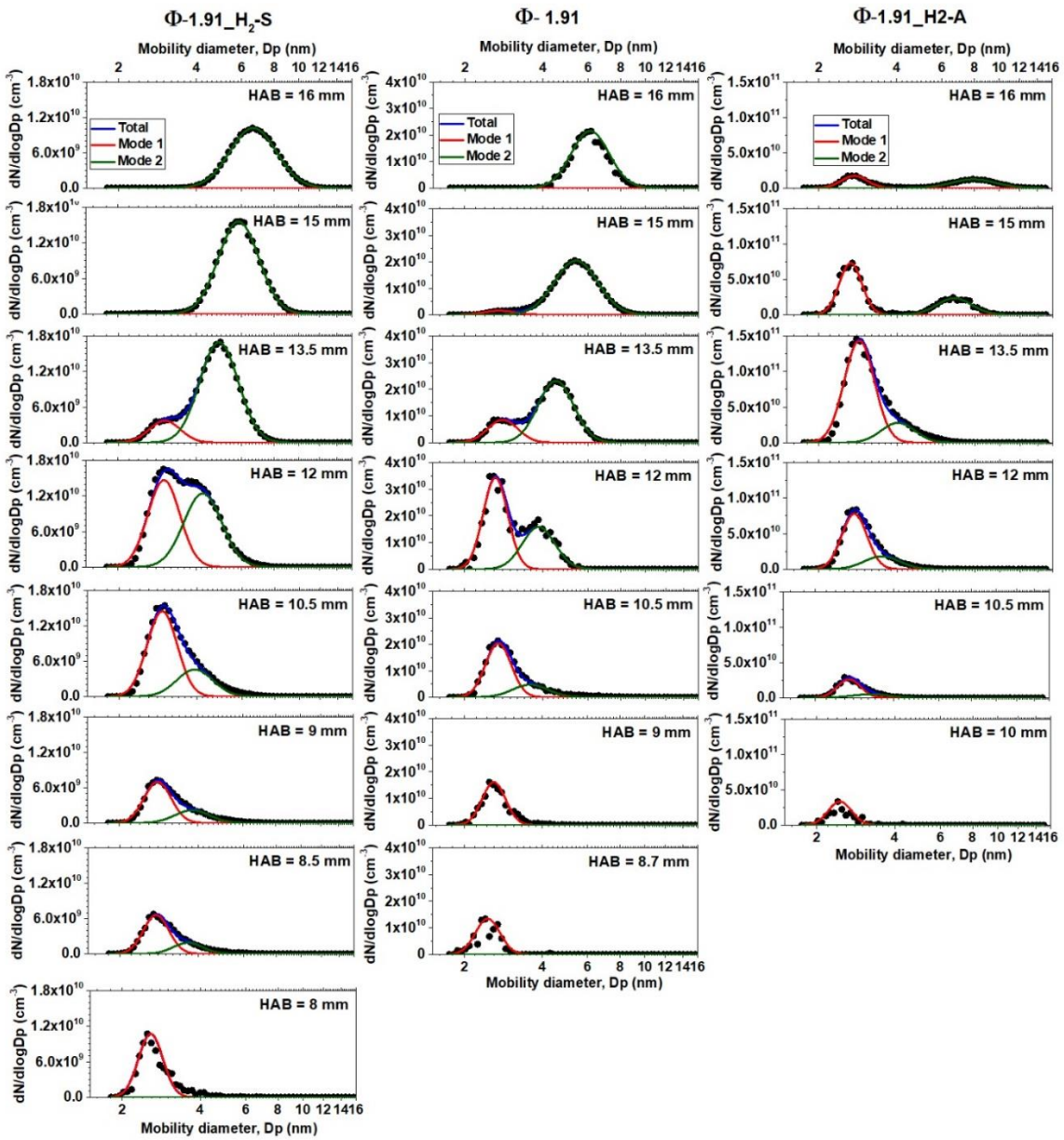

568 Fig. 8: Particles size distribution functions measured by SMPS, LII and CRDS obtained in the three

569 studied flames.

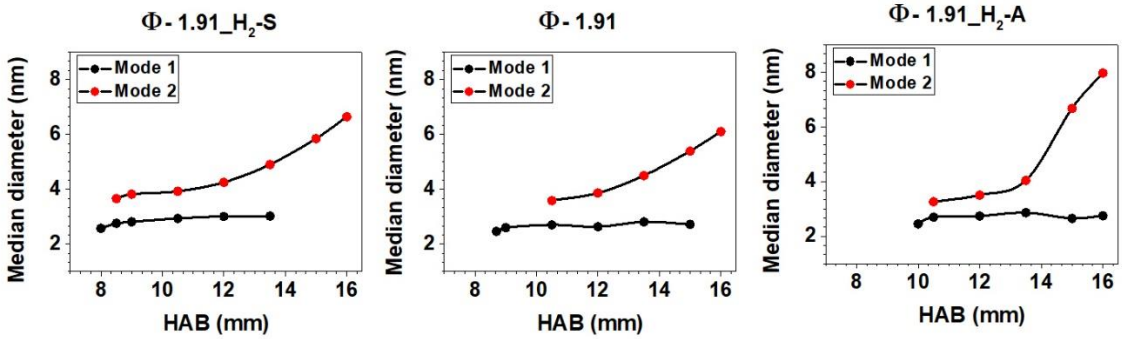

570 Fig. 9: Median diameter of mode 1 and mode 2 against HAB obtained by fitting the PSDFs in the three

571 studied flames.

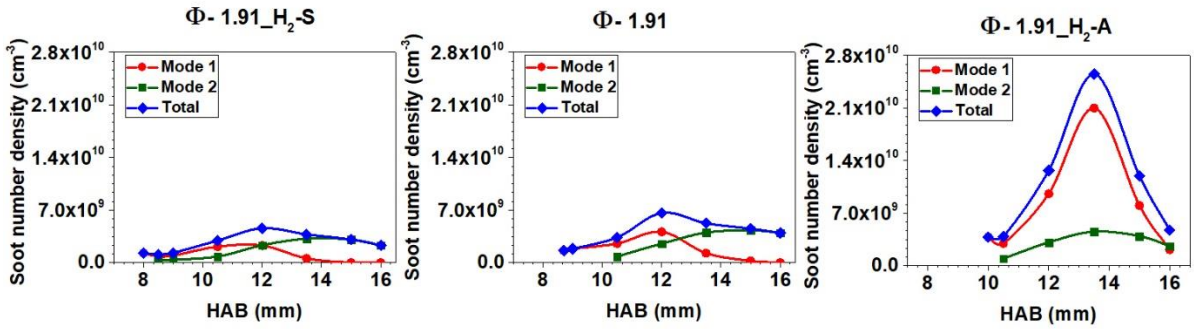

572

573 Fig. 10: Evolution of soot number density against HAB in the three studied flames.

574

575 Regarding the soot growth process, based on the evolution of the measured PSDFs (Fig.
576 8), we can deduce that the dynamic of these processes in the flame Φ-1.91_H_2-S is quite similar
577 to that in flame Φ-1.91. Indeed, mode 2 in this flame appears gradually as shown in Fig. 9, and
578 similarly the median diameter of mode 2 increases gradually at higher HAB. This suggests a
579 soot growth process mainly driven by surface growth processes as the HACA mechanism and
580 PAHs condensation on soot surface in these two flames. However, it is noteworthy that the H_2
581 substitution shifts the onset of the soot growth process to lower HAB than that in flame Φ-1.91.
582 Indeed, according to Fig. 6, the H_2 substitution also shifts to lower HAB the mole fraction
583 profile of soot precursors as C_2H_2 and aromatic species. The median diameter of mode 2 at 16
584 mm HAB in flame Φ-1.91_H_2-S is therefore slightly higher than in flame Φ-1.91 because the
585 residence time of soot particles for soot growth process in the flame Φ-1.91_H_2-S is slightly
586 longer than in the flame Φ-1.91. Finally, the H_2 substitution decreases the soot number density
587 of mode 2 and total soot number density because of the diminution of the initial quantity of
588 nascent soot particles formed in this flame.

589 In flame Φ-1.91_H_2-A, mode 2 initially appears very close to mode 1 at 10.5 mm HAB,
590 characterized by a median diameter evolving from 3.3 to 4.1 nm between 10.5 and 13.5 mm
591 HAB, similar to the reference flame. However, by contrast with the reference flame Φ-1.91, in
592 the Φ-1.91_H_2-A, mode 2 against HAB shows a substantial change of slope around 13.5 mm

HAB as shown in Fig. 9. The evolution of this mode, very different from that observed in the reference flame Φ-1.91, indicates the predominance of additional growth processes to those observed in the reference flame Φ-1.91, probably coagulation and/or coalescence. The sudden appearance of this mode 2 with median diameter 6.7 nm at 15 mm is indeed consistent with a stronger efficiency of the coagulation/coalescence processes of the particles of the mode 1 with a median diameter of 2.6 nm.

If this hypothesis is correct, the predominance of the coagulation/coalescence growth processes might be correlated with the larger number of soot particles formed in the flame Φ-1.91_H_2-A due to the addition of H_2 and therefore to the greater probability of particle collisions under these conditions. As shown in Fig. 10, H_2 addition strongly increases the number of soot particles of mode 1 compared to reference flame Φ-1.91, clearly highlighting the major role of H_2 in the nucleation process. The increase of nascent soot particles number density stops at 13.5 mm HAB and a drastic decrease of nascent soot particles is then observed between 13.5 and 15 mm HAB, directly correlated to the appearance of the isolated mode 2. It is interesting to note that this specific evolution only appears in this flame in which the quantity of nascent soot particles is up to 5 times higher than that in the reference flame Φ-1.91. The ensemble of the experimental data seems to suggest the existence of a threshold value for the particle concentrations above which the coagulation/coalescence processes would become dominant due to a greater probability of collision of soot particles. A complete understanding of this phenomena would require detailed modelling that was beyond the scope of this work and will be the subject of further investigations.

4.4.3. Effect of H_2 on nascent soot particles

As observed in Section 4.4.2, the H_2 addition induces a persistence of the soot nucleation process all along the flame height characterized by the presence of the mode 1 in substantial number density. To further explore the effect of H_2 addition on the nucleation process in sooting flame Φ-1.91, Fig.11 recaps the profiles of temperature, H_2, pyrene and soot number density of mode 1 in the two flames Φ-1.91, Φ-1.91_H_2-A.

As already stated, H_2 addition does not impact the temperature profile reported in Fig. 11a. Therefore, the observed modifications in the formation of aromatic species and soot reported in Fig.11c,d is rather related to the chemical effect due to the addition of H_2. We observe in Fig. 11b that the mole fraction of H_2 near the burner surface of flame Φ-1.91_H_2-A is higher than in the reference flame Φ-1.91 and tends to approach the mole fraction profile of H_2 of the reference flame from 8 mm up to 10.5 mm HAB (green area in the figure). The mole fraction of pyrene increases strongly in this zone due to the H_2 addition (Fig. 11c). As discussed earlier, the consumption of H atoms from the H_2 addition mainly serves to termination reactions involving aromatic radicals and yields stable aromatic compounds. Above 10.5 mm, the mole fraction of H_2 measured in the two flames Φ-1.91, Φ-1.91_H_2-A is similar. Therefore, the soot nucleation process after the pyrene peak is mainly impacted by a higher concentration of PAHs due to the H_2 addition, and resulting in the formation of a large number of nascent soot particles after the pyrene peak in flame Φ-1.91_H_2-A (10.5 – 13.5 mm, violet zone in the figure). The large number density of nascent soot particles at 13.5 mm HAB increases the coagulation/coalescence rate and results in the drastic reduction of the soot particles number density above this zone and the concomitant appearance of mode 2 centered around 6.7 nm at 15 mm HAB (see Fig. 8).

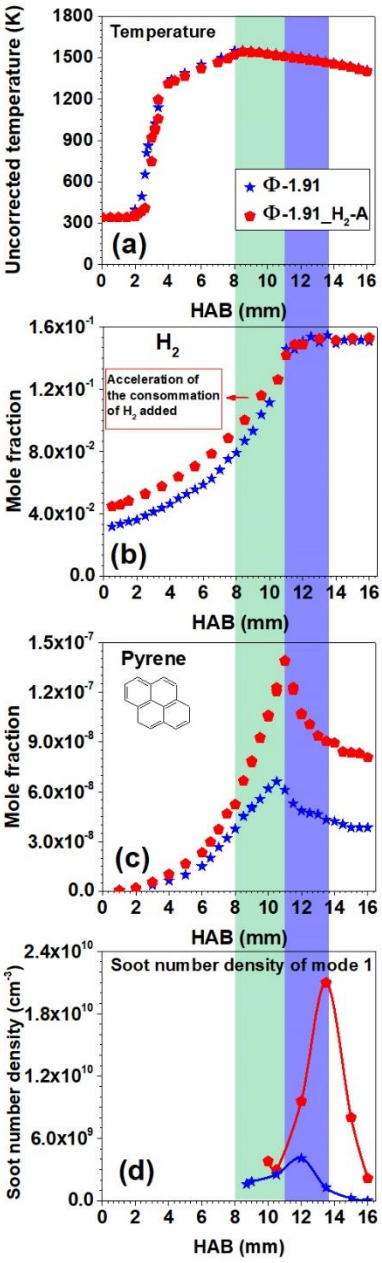

641

642 Fig. 11: Profiles of temperature, and mole fraction of H_2, pyrene and soot number density of mode 1 in
643 the two flames Φ-1.91 (blue), Φ-1.91_H_2-A (red). The green zone defines the accumulation of
644 aromatic species; the violet zone defines the consumption of aromatic species for nascent soot
645 formation. The line in Fig. 11d has been added to the plot to guide the eye.

646

647

This statement can be further corroborated by the analysis of previous experiments we carried out in slightly a sooting methane flame (Φ-1.82) [32] generating much less PAHs and soot particles than the Φ-1.91 flames. In this work, we also slightly perturbed the reference Φ-1.82 flame by H_2 addition or substitution according to the same protocol as used for the Φ-1.91. The PSDFs of the soot particles in these flames (not reported in [32]) was newly measured in the present work and reported in Fig. 12. The determination of the absolute soot number density N_p has been carried out according to the method described section 3.1, using the normalized PSDFs obtained by SMPS reported in SM1 (Fig. S8).

The Φ-1.82 reference flame has been defined as a nucleation flame, i.e. a flame generating soot particles which do not undergo or very limited growth processes all along the flame height. Hence, the soot PSDFs for this flame are characterized by almost one mode. As can been seen in SM1 (Fig. S9), this mode highlights a quasi-constant median diameter around 2.6 nm all along the flame height, similar to the mode 1 characterizing the nascent soot particles generated in the Φ-1.91 flames. A much weaker second mode however appears at 13.5 mm HAB, indicating that soot growth processes are still somewhat activated in the nucleation flame Φ-1.82, but actually well balanced by oxidation along a large part of the flame, precluding the growth of the soot particles excepted at the highest HABs [38].

According to Fig. 12, the introduction of H_2, either by addition or substitution, in these nucleation flames, does not impact the PSDF of the generated soot particles. By contrast, the introduction of H_2 in the nucleation flame Φ-1.82 strongly impacts the formation of aromatic species and soot volume fraction [32] as well as the soot number density as reported in Fig. 13. Similarly to the observations made for the Φ-1.91 flame, the H_2 substitution in the nucleation flame Φ-1.82 decreases the nascent soot particles number density while the H_2 addition strongly increases the nascent soot particles number density. However, the H_2 addition in the nucleation flame does not seem to modify the soot growth dynamic by enhancing the

coagulation/coalescence processes as observed in the richer flame Φ-1.91_H2-A, probably because of the much lower number density of soot particles (around 10 times less) generated in the flame Φ-1.82_H2-A in comparison with the Φ-1.91-A, therefore limiting the probability of collision of soot particles.

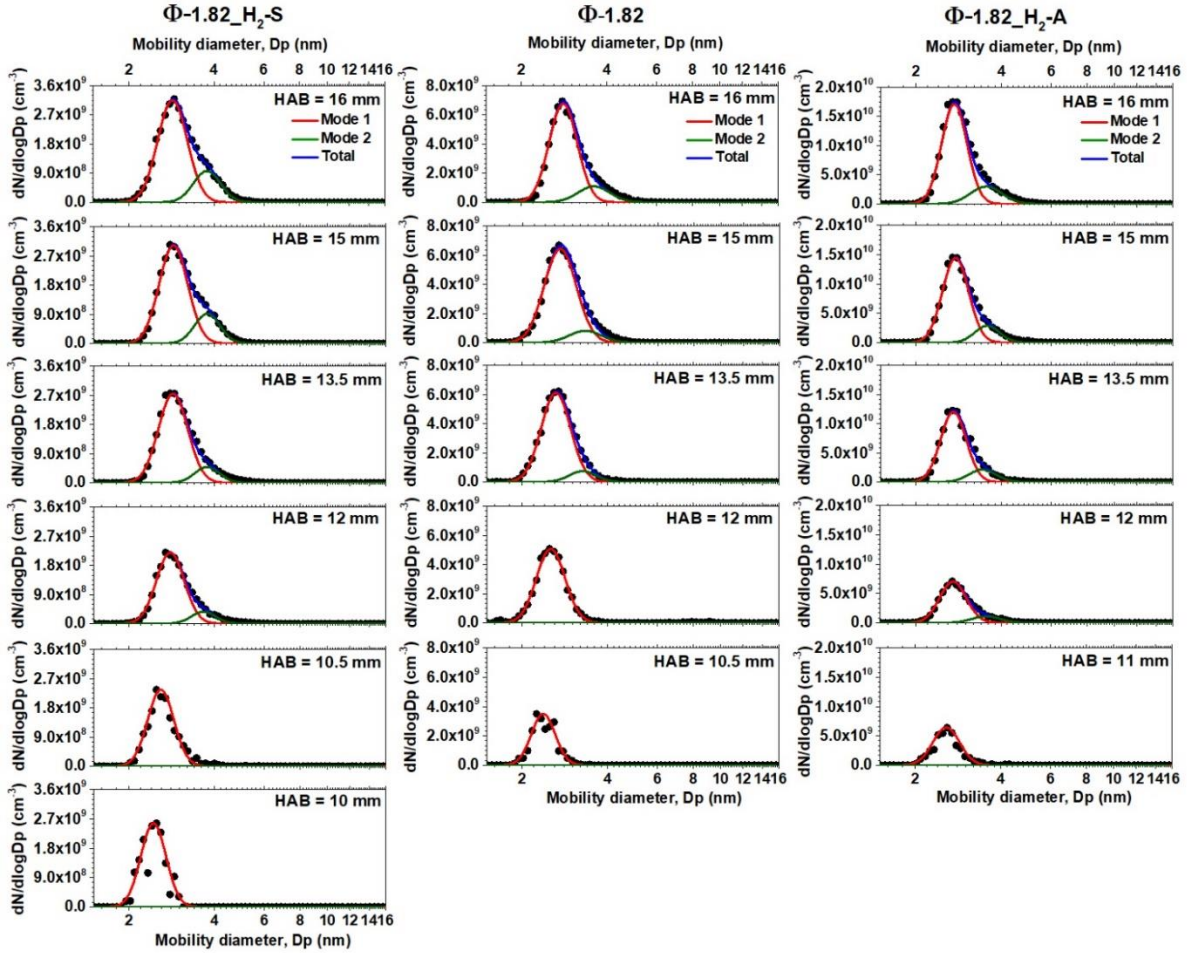

Fig. 12. Particles size distribution functions measured by SMPS obtained in the three methane nucleation flames.

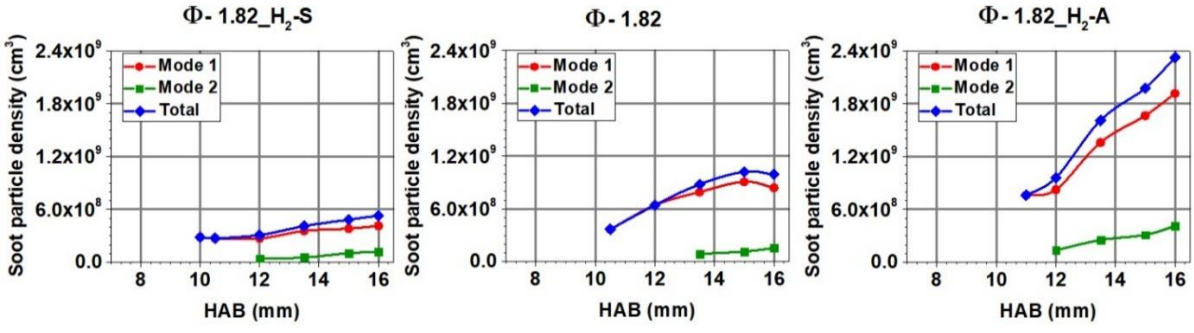

Fig. 13. Evolution of soot number density in the three methane nucleation flames.

5. Conclusion

This work reports new experimental data obtained in three atmospheric sooting premixed methane flames with and without added/substituted H_2 (~10% molar comparing to CH_4 fuel, at Φ_C=1.91). An original analytical methodology has been developed relying on the coupling of the data obtained by SMPS and LII/CRDS measurements to determine the soot number density. This method does not require accurate knowledge of the dilution in the sampling line, which is a strong limitation for quantitative SMSP measurements of particle number density.

Our results clearly show the influence of H_2 as a fuel additive to the formation of soot precursors, soot nucleation and soot growth. Similarly to previous observations on nucleation flames [32], the results obtained in the presented fuel-richer flames notably show that the introduction of H_2 strongly influences the concentration of aromatic species and soot, either increasing or decreasing, that depends on the operating conditions (H_2 addition or substitution). Finally, the invariance of the concentration of PAHs and the soot volume fraction measured at the beginning of the soot formation in the sooting flames Φ-1.91, similarly to previous experiments carried out in different nucleation flames, again supports the idea that onset of the soot particle might be controlled by specific concentrations thresholds of aromatic precursors already mentioned in [32].

Regarding the soot size distribution, we observed that neither H_2 substitution nor H_2 addition influence the PSDF and in particular the median diameter of mode 1 featuring the nascent particles either in the rich flames Φ-1.91 or in the nucleation flame Φ-1.82. This result indicates that the mechanism of nascent soot formation from gaseous precursors is probably similar in the three studied flames. The H_2 substitution in the flame does not influence the mechanism of soot growth, either. By contrast, we observe in the case of H_2 addition a substantial modification in the dynamic of the soot growth processes. This modification might

be due a better efficiency of the coagulation/coalescence processes because of the strong increase in the number of nascent soot particles. The H_2 addition indeed promotes the accumulation of PAHs in the area preceding the pyrene peak through termination reactions involving H atoms and PAH radicals. The accumulation of aromatic species prior to the pyrene peak provides a large reservoir of nascent soot particles molecular precursors resulting in the increase in the number of these particles after the pyrene peak. This large increase of the number of nascent soot particles in the Φ-1.91_H_2-A flame might therefore favor the coagulation/coalescence processes thus promoting their size increase in the burnt gas zone. From this study, we hypothesized the existence of a soot particle number density threshold above which the coagulation/coalescence processes might become more effective due to a greater probability of collision of soot particles. However, only the use of detailed soot growth models will enable an accurate description of the real dynamic and of the involved equilibria between the different soot growth processes taking place in these flames. This detailed modeling study will certainly be investigated in the near future.

Acknowledgements

This work was supported by the Agence Nationale de la Recherche through the LABEX CAPPA (ANR-11-LABX-0005), the Région Hauts-de-France, the Ministère de l'Enseignement Supérieur et de la Recherche (CPER Climibio) and the European Fund for Regional Economic Development.

References:

[1] Lin R-H, Ye Z-Z, Wu B-D. A review of hydrogen station location models. Int J Hydrog Energy 2020. https://doi.org/10.1016/j.ijhydene.2019.12.035.

[2] Shen X, Zhang C, Xiu G, Zhu H. Evolution of premixed stoichiometric hydrogen/air flame in a closed duct. Energy 2019;176:265–71. https://doi.org/10.1016/j.energy.2019.03.193.

[3] Xiao H, Duan Q, Sun J. Premixed flame propagation in hydrogen explosions. Renew Sustain Energy Rev 2018;81:1988–2001. https://doi.org/10.1016/j.rser.2017.06.008.

[4] Yang X, Wang T, Zhang Y, Zhang H, Wu Y, Zhang J. Hydrogen effect on flame extinction of hydrogen-enriched methane/air premixed flames: An assessment from the combustion safety point of view. Energy 2022;239:122248. https://doi.org/10.1016/j.energy.2021.122248.

[5] Jeon J, Kim SJ. Recent Progress in Hydrogen Flammability Prediction for the Safe Energy Systems. Energies 2020;13:6263. https://doi.org/10.3390/en13236263.

[6] Hao Q, Luo Z, Wang T, Xie C, Zhang S, Bi M, et al. The flammability limits and explosion behaviours of hydrogen-enriched methane-air mixtures. Exp Therm Fluid Sci 2021;126:110395. https://doi.org/10.1016/j.expthermflusci.2021.110395.

[7] Shen X, Xiu G, Wu S. Experimental study on the explosion characteristics of methane/air mixtures with hydrogen addition. Appl Therm Eng 2017;120:741–7. https://doi.org/10.1016/j.applthermaleng.2017.04.040.

[8] Zhang C, Shen X, Wen JX, Xiu G. The behavior of methane/hydrogen/air premixed flame in a closed channel with inhibition. Fuel 2020;265:116810. https://doi.org/10.1016/j.fuel.2019.116810.

[9] Karim GA. Hydrogen as a spark ignition engine fuel. Int J Hydrog Energy 2003;28:569–77. https://doi.org/10.1016/S0360-3199(02)00150-7.

[10] de Ferrières S, El Bakali A, Lefort B, Montero M, Pauwels JF. Experimental and numerical investigation of low-pressure laminar premixed synthetic natural gas/O2/N2 and natural gas/H2/O2/N2 flames. Combust Flame 2008;154:601–23. https://doi.org/10.1016/j.combustflame.2008.04.018.

[11] Kumar P, Mishra DP. Experimental investigation of laminar LPG–H2 jet diffusion flame. Int J Hydrog Energy 2008;33:225–31. https://doi.org/10.1016/j.ijhydene.2007.09.023.

[12] Deng S, Mueller ME, Chan QN, Qamar NH, Dally BB, Alwahabi ZT, et al. Hydrodynamic and chemical effects of hydrogen addition on soot evolution in turbulent nonpremixed bluff body ethylene flames. Proc Combust Inst 2017;36:807–14. https://doi.org/10.1016/j.proci.2016.09.004.

[13] Choudhuri AR, Gollahalli SR. Laser induced fluorescence measurements of radical concentrations in hydrogen–hydrocarbon hybrid gas fuel flames. Int J Hydrog Energy 2000;25:1119–27. https://doi.org/10.1016/S0360-3199(00)00025-2.

[14] Tesner PA, Robinovitch HJ, Rafalkes IS. The formation of dispersed carbon in hydrocarbon diffusion flames. Symp Int Combust 1961;8:801–6. https://doi.org/10.1016/S0082-0784(06)80575-8.

[15] Du DX, Axelbaum RL, Law CK. Soot formation in strained diffusion flames with gaseous additives. Combust Flame 1995;102:11–20. https://doi.org/10.1016/0010-2180(95)00043-6.

[16] Choi J-H, Hwang C-H, Choi SK, Lee SM, Lee WJ, Jang SH, et al. Impacts of hydrogen addition on micro and nanostructure of soot particles formed in C2H4/air counter diffusion flames. Int J Hydrog Energy 2016;41:15852–8. https://doi.org/10.1016/j.ijhydene.2016.04.158.

[17] Gülder ÖL, Snelling DR, Sawchuk RA. Influence of hydrogen addition to fuel on temperature field and soot formation in diffusion flames. Symp Int Combust 1996;26:2351–8. https://doi.org/10.1016/S0082-0784(96)80064-6.
[18] Glassman I. Sooting laminar diffusion flames: Effect of dilution, additives, pressure, and microgravity. Symp Int Combust 1998;27:1589–96. https://doi.org/10.1016/S0082-0784(98)80568-7.
[19] Guo H, Liu F, Smallwood GJ, Gülder ÖL. Numerical study on the influence of hydrogen addition on soot formation in a laminar ethylene–air diffusion flame. Combust Flame 2006;145:324–38. https://doi.org/10.1016/j.combustflame.2005.10.016.
[20] Gu M, Chu H, Liu F. Effects of simultaneous hydrogen enrichment and carbon dioxide dilution of fuel on soot formation in an axisymmetric coflow laminar ethylene/air diffusion flame. Combust Flame 2016;166:216–28. https://doi.org/10.1016/j.combustflame.2016.01.023.
[21] Sun Z, Dally B, Nathan G, Alwahabi Z. Effects of hydrogen and nitrogen on soot volume fraction, primary particle diameter and temperature in laminar ethylene/air diffusion flames. Combust Flame 2017;175:270–82. https://doi.org/10.1016/j.combustflame.2016.08.031.
[22] Zhao H, Stone R, Williams B. Investigation of the soot formation in ethylene laminar diffusion flames when diluted with helium or supplemented by hydrogen. Energy Fuels 2014;28:2144–51. https://doi.org/10.1021/ef401970q.
[23] Pandey P, Pundir BP, Panigrahi PK. Hydrogen addition to acetylene–air laminar diffusion flames: Studies on soot formation under different flow arrangements. Combust Flame 2007;148:249–62. https://doi.org/10.1016/j.combustflame.2006.09.004.
[24] De Iuliis S, Maffi S, Migliorini F, Cignoli F, Zizak G. Effect of hydrogen addition on soot formation in an ethylene/air premixed flame. Appl Phys B 2012;106:707–15. https://doi.org/10.1007/s00340-012-4903-2.
[25] Haynes BS, Jander H, Mätzing H, Wagner HGg. The influence of gaseous additives on the formation of soot in premixed flames. Symp Int Combust 1982;19:1379–85. https://doi.org/10.1016/S0082-0784(82)80314-7.
[26] Wei M, Liu J, Guo G, Li S. The effects of hydrogen addition on soot particle size distribution functions in laminar premixed flame. Int J Hydrog Energy 2016;41:6162–9. https://doi.org/10.1016/j.ijhydene.2015.10.022.
[27] Park S-H, Lee K-M, Hwang C-H. Effects of hydrogen addition on soot formation and oxidation in laminar premixed C2H2/air flames. Int J Hydrog Energy 2011;36:9304–11. https://doi.org/10.1016/j.ijhydene.2011.05.031.
[28] Ezenwajiaku C, Talibi M, Doan NAK, Swaminathan N, Balachandran R. Study of polycyclic aromatic hydrocarbons (PAHs) in hydrogen-enriched methane diffusion flames. Int J Hydrog Energy 2019;44:7642–55. https://doi.org/10.1016/j.ijhydene.2019.01.253.
[29] Mze Ahmed A, Mancarella S, Desgroux P, Gasnot L, Pauwels J-F, El Bakali A. Experimental and numerical study on rich methane/hydrogen/air laminar premixed flames at atmospheric pressure: Effect of hydrogen addition to fuel on soot gaseous precursors. Int J Hydrog Energy 2016;41:6929–42. https://doi.org/10.1016/j.ijhydene.2015.11.148.
[30] Liu F, Ai Y, Kong W. Effect of hydrogen and helium addition to fuel on soot formation in an axisymmetric coflow laminar methane/air diffusion flame. Int J Hydrog Energy 2014;39:3936–46. https://doi.org/10.1016/j.ijhydene.2013.12.151.
[31] Xu L, Yan F, Wang Y, Chung SH. Chemical effects of hydrogen addition on soot formation in counterflow diffusion flames: Dependence on fuel type and oxidizer composition. Combust Flame 2020;213:14–25. https://doi.org/10.1016/j.combustflame.2019.11.011.

[32] Do H-Q, Tran L-S, Gasnot L, Mercier X, El Bakali A. Experimental study of the influence of hydrogen as a fuel additive on the formation of soot precursors and particles in atmospheric laminar premixed flames of methane. Fuel 2021;287:119517. https://doi.org/10.1016/j.fuel.2020.119517.
[33] Frenklach M, Feigelson ED. Formation of Polycyclic Aromatic Hydrocarbons in Circumstellar Envelopes. Astrophys J 1989;341:372. https://doi.org/10.1086/167501.
[34] Frenklach M, Gardiner W c, Stein S e., Clary D w., Yuan T. Mechanism of Soot Formation in Acetylene-Oxygen Mixtures. Combust Sci Technol 1986;50:79–115. https://doi.org/10.1080/00102208608923927.
[35] Frenklach M, Yuan T, Ramachandra MK. Soot formation in binary hydrocarbon mixtures. Energy Fuels 1988;2:462–80. https://doi.org/10.1021/ef00010a013.
[36] Dearden P, Long R. Soot formation in ethylene and propane diffusion flames. J Appl Chem 1968;18:243–51. https://doi.org/10.1002/jctb.5010180805.
[37] Wang Y, Gu M, Gao Y, Liu X, Lin Y. An experimental and numerical study of soot formation of laminar coflow H2/C2H4 diffusion flames in O2CO2 atmosphere. Combust Flame 2020;221:50–63. https://doi.org/10.1016/j.combustflame.2020.07.026.
[38] Desgroux P, Faccinetto A, Mercier X, Mouton T, Aubagnac Karkar D, El Bakali A. Comparative study of the soot formation process in a “nucleation” and a “sooting” low pressure premixed methane flame. Combust Flame 2017;184:153–66. https://doi.org/10.1016/j.combustflame.2017.05.034.
[39] Gaseq Chemical Equilibrium Program n.d. http://www.gaseq.co.uk/ (accessed February 28, 2020).
[40] Smith GP, Golden DM, Frenklach M, Moriarty NW, Eiteneer B, Goldenberg M, et al. GRI-Mech 3.0, URL: <http://www.me.berkeley.edu/gri_mech> 51; 1999 p.55 n.d.
[41] Kint JH. A noncatalytic coating for platinum-rhodium thermocouples. Combust Flame 1970;14:279–81. https://doi.org/10.1016/S0010-2180(70)80040-2.
[42] Betrancourt C, Mercier X, Liu F, Desgroux P. Quantitative measurement of volume fraction profiles of soot of different maturities in premixed flames by extinction-calibrated laser-induced incandescence. Appl Phys B 2019;125:16. https://doi.org/10.1007/s00340-018-7127-2.
[43] Mouton T, Mercier X, Wartel M, Lamoureux N, Desgroux P. Laser-induced incandescence technique to identify soot nucleation and very small particles in low-pressure methane flames. Appl Phys B 2013;112:369–79. https://doi.org/10.1007/s00340-013-5446-x.
[44] Bladh H, Olofsson N-E, Mouton T, Simonsson J, Mercier X, Faccinetto A, et al. Probing the smallest soot particles in low-sooting premixed flames using laser-induced incandescence. Proc Combust Inst 2015;35:1843–50. https://doi.org/10.1016/j.proci.2014.06.001.
[45] Olofsson N-E, Johnsson J, Bladh H, Bengtsson P-E. Soot sublimation studies in a premixed flat flame using laser-induced incandescence (LII) and elastic light scattering (ELS). Appl Phys B 2013;112:333–42. https://doi.org/10.1007/s00340-013-5509-z.
[46] Liu F, Yon J, Fuentes A, Lobo P, Smallwood GJ, Corbin JC. Review of recent literature on the light absorption properties of black carbon: Refractive index, mass absorption cross section, and absorption function. Aerosol Sci Technol 2020;54:33–51. https://doi.org/10.1080/02786826.2019.1676878.
[47] Török S, Mannazhi M, Bengtsson P-E. Laser-induced incandescence (2λ and 2C) for estimating absorption efficiency of differently matured soot. Appl Phys B 2021;127:96. https://doi.org/10.1007/s00340-021-07638-1.
[48] Olofsson N-E, Simonsson J, Török S, Bladh H, Bengtsson P-E. Evolution of properties for aging soot in premixed flat flames studied by laser-induced incandescence and elastic

light scattering. Appl Phys B 2015;119:669–83. https://doi.org/10.1007/s00340-015-6067-3.
[49] Johansson KO, El Gabaly F, Schrader PE, Campbell MF, Michelsen HA. Evolution of maturity levels of the particle surface and bulk during soot growth and oxidation in a flame. Aerosol Sci Technol 2017;51:1333–44. https://doi.org/10.1080/02786826.2017.1355047.
[50] Migliorini F, Thomson KA, Smallwood GJ. Investigation of optical properties of aging soot. Appl Phys B 2011;104:273–83. https://doi.org/10.1007/s00340-011-4396-4.
[51] Yon J, Cruz JJ, Escudero F, Morán J, Liu F, Fuentes A. Revealing soot maturity based on multi-wavelength absorption/emission measurements in laminar axisymmetric coflow ethylene diffusion flames. Combust Flame 2021;227:147–61. https://doi.org/10.1016/j.combustflame.2020.12.049.
[52] Bladh H, Johnsson J, Olofsson N-E, Bohlin A, Bengtsson P-E. Optical soot characterization using two-color laser-induced incandescence (2C-LII) in the soot growth region of a premixed flat flame. Proc Combust Inst 2011;33:641–8. https://doi.org/10.1016/j.proci.2010.06.166.
[53] Lemaire R, Menanteau S. Modeling laser-induced incandescence of Diesel soot—Implementation of an advanced parameterization procedure applied to a refined LII model accounting for shielding effect and multiple scattering within aggregates for alphaT and E(m) assessment. Appl Phys B 2021;127:138. https://doi.org/10.1007/s00340-021-07665-y.
[54] Yon J, Lemaire R, Therssen E, Desgroux P, Coppalle A, Ren KF. Examination of wavelength dependent soot optical properties of diesel and diesel/rapeseed methyl ester mixture by extinction spectra analysis and LII measurements. Appl Phys B 2011;104:253–71. https://doi.org/10.1007/s00340-011-4416-4.
[55] Betrancourt C, Liu F, Desgroux P, Mercier X, Faccinetto A, Salamanca M, et al. Investigation of the size of the incandescent incipient soot particles in premixed sooting and nucleation flames of n-butane using LII, HIM, and 1 nm-SMPS. Aerosol Sci Technol 2017;51:916–35. https://doi.org/10.1080/02786826.2017.1325440.
[56] Tang Q, Cai R, You X, Jiang J. Nascent soot particle size distributions down to 1nm from a laminar premixed burner-stabilized stagnation ethylene flame. Proc Combust Inst 2017;36:993–1000. https://doi.org/10.1016/j.proci.2016.08.085.
[57] 1nm Scanning Mobility Particle Sizer Spectrometer 3938E57 - n.d. https://tsi.com/products/particle-sizers/particle-size-spectrometers/1nm-scanning-mobility-particle-sizer-spectrometer-3938e57/ (accessed October 6, 2019).
[58] Maricq MM, Harris SJ, Szente JJ. Soot size distributions in rich premixed ethylene flames. Combust Flame 2003;132:328–42. https://doi.org/10.1016/S0010-2180(02)00502-3.
[59] Tang Q, Ge B, Ni Q, Nie B, You X. Soot formation characteristics of n-heptane/toluene mixtures in laminar premixed burner-stabilized stagnation flames. Combust Flame 2018;187:239–46. https://doi.org/10.1016/j.combustflame.2017.08.022.
[60] Gu C, Lin H, Camacho J, Lin B, Shao C, Li R, et al. Particle size distribution of nascent soot in lightly and heavily sooting premixed ethylene flames. Combust Flame 2016;165:177–87. https://doi.org/10.1016/j.combustflame.2015.12.002.
[61] Lin H, Gu C, Camacho J, Lin B, Shao C, Li R, et al. Mobility size distributions of soot in premixed propene flames. Combust Flame 2016;172:365–73. https://doi.org/10.1016/j.combustflame.2016.07.002.
[62] Abid AD, Camacho J, Sheen DA, Wang H. Evolution of Soot Particle Size Distribution Function in Burner-Stabilized Stagnation n-Dodecane−Oxygen−Argon Flames. Energy Fuels 2009;23:4286–94. https://doi.org/10.1021/ef900324e.

[63] Lin B, Gu H, Guan B, Han D, Gu C, Huang Z, et al. Size evolution of soot particles from gasoline and n-heptane/toluene blend in a burner stabilized stagnation flame. Fuel 2017;203:135–44. https://doi.org/10.1016/j.fuel.2017.04.097.
[64] Wu J, Faccinetto A, Grimonprez S, Batut S, Yon J, Desgroux P, et al. Influence of the dry aerosol particle size distribution and morphology on the cloud condensation nuclei activation. An experimental and theoretical investigation. Atmospheric Chem Phys 2020;20:4209–25. https://doi.org/10.5194/acp-20-4209-2020.
[65] Kulkarni P, Baron PA, Willeke K. Aerosol Measurement: Principles, Techniques, and Applications. John Wiley & Sons, Inc 2011. https://onlinelibrary.wiley.com/doi/book/10.1002/9781118001684.
[66] Birmili W, Stratmann F, Wiedensohler A, Covert D, Russell LM, Berg O. Determination of Differential Mobility Analyzer Transfer Functions Using Identical Instruments in Series. Aerosol Sci Technol 1997;27:215–23. https://doi.org/10.1080/02786829708965468.
[67] Chen D-R, Pui DYH, Hummes D, Fissan H, Quant FR, Sem GJ. Design and evaluation of a nanometer aerosol differential mobility analyzer (Nano-DMA). J Aerosol Sci 1998;29:497–509. https://doi.org/10.1016/S0021-8502(97)10018-0.
[68] Richter H, Howard JB. Formation of polycyclic aromatic hydrocarbons and their growth to soot—a review of chemical reaction pathways. Prog Energy Combust Sci 2000;26:565–608. https://doi.org/10.1016/S0360-1285(00)00009-5.
[69] Frenklach M. On the driving force of PAH production. Symp Int Combust 1989;22:1075–82. https://doi.org/10.1016/S0082-0784(89)80117-1.
[70] El Bakali A, Mercier X, Wartel M, Acevedo F, Burns I, Gasnot L, et al. Modeling of PAHs in low pressure sooting premixed methane flame. Energy 2012;43:73–84. https://doi.org/10.1016/j.energy.2011.12.026.
[71] Frenklach M. Reaction mechanism of soot formation in flames. Phys Chem Chem Phys 2002;4:2028–37. https://doi.org/10.1039/B110045A.
[72] Mercier X, Carrivain O, Irimiea C, Faccinetto A, Therssen E. Dimers of polycyclic aromatic hydrocarbons: the missing pieces in the soot formation process. Phys Chem Chem Phys 2019;21:8282–94. https://doi.org/10.1039/C9CP00394K.
[73] Aubagnac-Karkar D, El Bakali A, Desgroux P. Soot particles inception and PAH condensation modelling applied in a soot model utilizing a sectional method. Combust Flame 2018;189:190–206. https://doi.org/10.1016/j.combustflame.2017.10.027.
[74] Kholghy MR, Kelesidis GA, Pratsinis SE. Reactive polycyclic aromatic hydrocarbon dimerization drives soot nucleation. Phys Chem Chem Phys 2018;20:10926–38. https://doi.org/10.1039/C7CP07803J.
[75] Commodo M, De Falco G, Bruno A, Borriello C, Minutolo P, D'Anna A. Physicochemical evolution of nascent soot particles in a laminar premixed flame: from nucleation to early growth. Combust Flame 2015;162:3854–63. https://doi.org/10.1016/j.combustflame.2015.07.022.
[76] Abid AD, Heinz N, Tolmachoff ED, Phares DJ, Campbell CS, Wang H. On evolution of particle size distribution functions of incipient soot in premixed ethylene–oxygen–argon flames. Combust Flame 2008;154:775–88. https://doi.org/10.1016/j.combustflame.2008.06.009.
[77] Zhao B, Yang Z, Johnston MV, Wang H, Wexler AS, Balthasar M, et al. Measurement and numerical simulation of soot particle size distribution functions in a laminar premixed ethylene-oxygen-argon flame. Combust Flame 2003;133:173–88. https://doi.org/10.1016/S0010-2180(02)00574-6.
[78] Abid AD, Heinz N, Tolmachoff ED, Phares DJ, Campbell CS, Wang H. On evolution of particle size distribution functions of incipient soot in premixed ethylene–oxygen–argon

flames. Combust Flame 2008;154:775–88. https://doi.org/10.1016/j.combustflame.2008.06.009.
[79] Balthasar M, Frenklach M. Detailed kinetic modeling of soot aggregate formation in laminar premixed flames. Combust Flame 2005;140:130–45. https://doi.org/10.1016/j.combustflame.2004.11.004.

Figure Captions:

Fig.1: Normalized fluence curves at 0.2 J/cm^2 obtained in three studied flames. Φ-1.91: CH_4 sooting reference flame; Φ-1.91_H_2-S: CH_4 substituted-H_2 flame; Φ-1.91_H_2-A: CH_4 added-H_2 flame.

Fig. 2: Result of the fitting procedure by using two lognormal functions at the onset of the bimodality of size distribution at 12 mm HAB in sooting flame Φ-1.91.

Fig. 3: Determination of number density of mode 1 and 2 of soot particles at 12 mm HAB in the flame Φ-1.91.

Fig. 4: Impact of H_2 on the uncorrected flame temperature profiles. Φ-1.91: CH_4 flame; Φ-1.91_H_2-S: CH_4 substituted-H_2 flame; Φ-1.91_H_2-A: CH_4 added-H_2 flame (see Table 1 for the flame conditions).

Fig. 5: Mole fraction profiles of reactants (fuel, O_2) and major products (CO, CO_2, H_2, H_2O) obtained in the three studied flames.

Fig. 6: Mole fraction profiles of aliphatic species (acetylene, allene, propyne) and aromatic species (benzene, naphthalene and pyrene) obtained in the three studied flames.

Fig.7: Soot volume fraction profiles measured in the three studied flames by LII /CRDS. (a) log scale and (b) linear scale.

Fig. 8: Particles size distribution functions measured by SMPS, LII and CRDS obtained in the three studied flames.

Fig. 9: Median diameter of mode 1 and mode 2 against HAB obtained by fitting the PSDFs in the three studied flames.

Fig. 10: Evolution of soot number density against HAB in the three studied flames.

Fig. 11: Profiles of temperature, and mole fraction of H_2, pyrene and soot number density of mode 1 in the two flames Φ-1.91 (blue), Φ-1.91_H_2-A (red). The green zone defines the

accumulation of aromatic species; the violet zone defines the consumption of aromatic species for nascent soot formation. The line in Fig. 11d has been added to the plot to guide the eye.

Fig. 12. Particles size distribution function measured by SMPS obtained in the three methane nucleation flames.

Fig. 13. Evolution of soot number density in the three methane nucleation flames.